Mechanical properties, corrosion performance and cell viability studies on newly developed porous Fe-Mn-Si-Pd alloys

Y. P. Feng[1], N. Gaztelumendi [2], J. Fornell[1,*], H. Y. Zhang[1], P. Solsona[1], M. D. Baró[1], S. Suriñach[1], E. Ibáñez[2], L. Barrios[2], E. Pellicer[1,§], C. Nogués[2], J. Sort[1,3]

[1]*Departament de Física, Universitat Autònoma de Barcelona, E-08193 Bellaterra, Cerdanyola del Vallès, Spain*

[2]*Departament de Biologia Cel·lular, Fisiologia i Immunologia, Universitat Autònoma de Barcelona, E-08193 Bellaterra, Cerdanyola del Vallès, Spain*

[3] *ICREA, Pg. Lluís Companys 23, E-08010 Barcelona, Spain*

Corresponding author. E-mail addresses:

*Jordina.Fornell@uab.cat, §Eva.Pellicer@uab.cat

***Keywords*:** Porous Alloys, Open-cell Fe-based foam, Space holder, Mechanical properties, Biomaterials, Cytotoxicity

ABSTRACT

Porous Fe-30Mn6Si1Pd (wt.%) alloys were prepared by a simple press and sinter process from ball-milled Fe, Mn, Si and Pd powders blended with 10 wt.%, 20 wt.% and 40 wt.% NaCl to obtain different degrees of porosity. For comparison purposes, a bulk fully-compact Fe-30Mn6Si1Pd alloy was produced by arc-melting and subsequent copper-mold suction-casting. While the porous Fe-30Mn6Si1Pd alloys only consist of γ-austenite, their fully-compact counterpart comprises ε-martensite and γ-austenite phases. In all cases, the low magnetic susceptibility response assures good compatibility with nuclear magnetic resonance and magnetic resonance imaging techniques. Furthermore, a reduction of the Young's modulus, from 55 to 7 GPa, was attained by introducing porosity. The biodegradation performance was evaluated by static immersion and electrochemical corrosion tests in Hank's solution. The influence of immersion time on composition, microstructure, mechanical and magnetic properties was assessed. While introducing porosity renders alloys with suitable mechanical and magnetic properties, it also has a detrimental effect in terms of cell viability. Hence, the porosity level needs to be controlled in order to obtain alloys with an optimized performance.

1. Introduction

The development of metallic materials for permanent implant applications such as Ti alloys, 316L stainless steels and Co-Cr alloy has been a subject of intense research in recent years because of their high corrosion resistance, good biocompatibility and excellent mechanical properties [1-3]. However, a secondary surgery for implant removal is often necessary to avoid long-term complications, such as chronic inflammation, possible subsequent thrombosis and systemic toxicity [4,5]. To overcome this drawback, biodegradable metallic implants emerged as a novel class of biomaterials, improving the patient's comfort and reducing the cost of medical treatment [6-12].

Mg-based and Fe-based alloys are the two main types of biodegradable metallic materials considered as potential candidates for temporary medical biodegradable implants, such as stents or bone replacements [6-9]. Mg-based degradable alloys have been, by far, the most extensively explored ones because of their fast biodegradability and Young's modulus closer to that of human bone. However, the degradation rate of Mg-based biomaterials in the human body is typically exceedingly fast and this causes a loss of their mechanical integrity before the patient fully recovers. Another issue with Mg-based biomaterials is the considerable amount of hydrogen release, which prolongs the healing process and impedes a good connectivity between osteocytes and the implant. To tackle these issues, in the last few years, more attention is being paid to Fe-based alloys. Typically, Fe-based alloys exhibit good biocompatibility and competitive mechanical properties; however, in most cases, their degradation in the human body is too slow. The most explored approach to increase their degradation rate without compromising the strength is the addition of certain biocompatible elements (i.e., P, Mn, Pd, etc.) [6,10-14]. Furthermore, a careful selection of potential alloying elements is required to avoid non-ferromagnetic properties, which would hinder the utilization of nuclear magnetic resonance (NMR) or magnetic resonance imaging (MRI) techniques, required to monitor the patient's recovery after surgery.

Within this framework, FeMn-based alloys [6,10-18] emerged as new materials for biodegradable implants and stents. FeMn alloys with 20-35 wt.% Mn (with γ-austenite and ε-martensite microstructures), show a reduced magnetic susceptibility compared to 316L steel

[18]. Furthermore, the addition of Mn within the solubility limit of Fe reduces the standard electrode potential of Fe to make it more susceptible to corrosion [11,14]. Therefore, Fe alloys containing 20-35 wt.% Mn have been investigated for their potential use as biodegradable implant and stent applications. On the other hand, silicon can increase the strength of the alloy and it is expected to assist the healing process while not causing deleterious effects in the immunologic system, since silicon is an essential mineral in the human body [17,19]. Fe-Mn-Si alloy has been studied for a long time [14,17] because of its shape memory behavior, which may also be of interest for some applications in the biomedical field (e.g., stents) [17].

In our previous study [14], a bulk, fully-compact, Fe-30Mn6Si1Pd alloy was fabricated by arc-melting and copper-mold suction casting. The alloy demonstrated satisfactory magnetic, corrosion properties and good cell viability and proliferation; however, its Young's modulus was too high (93 GPa) when compared to that of the human bone (3-25 GPa) [20]. Making the material porous is an effective way to lower the Young's modulus, as the Young's modulus (and the yield stress) are both proportional to the relative density of the material [21]. Namely, both hardness and Young's modulus progressively decrease with the increase of porosity. Furthermore, porosity increases the overall available surface area of the material to the corrosive environment, which might enhance the degradation process.

In the present work, porous Fe-30Mn6Si1Pd alloys were prepared by a simple press and sinter process from ball-milled Fe, Mn, Si and Pd powders blended with 10 wt.%, 20 wt.% and 40 wt.% NaCl, as space-holding material, rendering different porosity degrees, once NaCl is removed by thermal treatments (sublimation). The obtained open-cell porous FeMnSiPd materials are compared with the bulk fully-compact one synthesized by arc-melting and subsequent copper-mold suction-casting, paying particular attention to the resulting magnetic, mechanical, corrosion resistance and biocompatibility properties. The evolution of the microstructure, the mechanical and the magnetic properties during the course of immersion experiments has also been investigated. Moreover, the eventual cytotoxicity of all these alloys has been assessed in terms of cell viability and cell proliferation. Experiments were performed by culturing the cells during 14 days in conditioned media derived from bulk and porous alloys.

2. Materials and methods

2.1. Materials

Commercial Fe (97%), Si (99%), Mn (99%) and Pd (99.95%) powders were used as starting materials. First, the powders were mixed and mechanically milled in a planetary mill device (Fritsch Pulverisette 5) to obtain the targeted composition, Fe-30Mn6Si1Pd (nominal wt.%). To avoid Mn sublimation, the raw powders were milled under Ar atmosphere with a ball-to-powder weight ratio of 10:1 at 300 rpm for 15 h to induce mechanical alloying. The XRD patterns of the powders milled for 1, 3 and 15 h are shown in Figure S1. The particle size of the as-milled powders, calculated from an SEM image using the ImageJ software, was 10.8 ± 1.4 μm. Then, the powders were further mixed with 10 wt.%, 20 wt.% or 40 wt.% NaCl (which will later act as a source of porosity) and milled at 200 rpm for 2 h, to ensure homogeneity. All the operations prior to milling (weighting of the powder and sealing of the container) were done in a glove box under Ar atmosphere (<0.2 O_2 ppm, <0.1 H_2O ppm) to avoid oxidation and any other atmospheric contamination. Subsequently, the prepared powder mixtures were uniaxially pressed under a pressure of 100 MPa to obtain pellets of 9 mm in diameter and 2-3 mm in thickness. The NaCl-containing green compacts were loaded in a vacuum furnace and sintered at 900 °C at $5 \cdot 10^{-5}$ mbar for 4 h at a heating rate of 1 °C/min. Because of the hight vapor pressure of Mn, larger sintering temperatures and dwelling times will result in noticeable Mn loss as pointed out by other authors [22,23]. During this process NaCl sublimated, leaving numerous pores beneath. The resulting samples are denoted as Fe-30Mn6Si1Pd-10%NaCl, Fe-30Mn6Si1Pd-20%NaCl and Fe-30Mn6Si1Pd-40%NaCl throughout the manuscript to indicate the parent amount of NaCl used as porogen. The crystal size of NaCl and the pore size of the resulting samples was measured using the Image J software. Density of the sintered samples and hence, the total porosity was calculated according to the Archimedes' principle.

For comparison purposes, a fully-compact Fe-30Mn6Si1Pd alloy (nominal composition) was also produced by arc-melting and subsequent suction-casting. The experimental details concerning the synthesis of this sample are described elsewhere [14]. Optical images comparing the appearance of the bulk fully-compact Fe-30Mn6Si1Pd and Fe-30Mn6Si1Pd-40%NaCl porous alloys are shown in Figure 1.

The real composition of the as-prepared samples, measured by energy dispersive X-ray spectroscopy (EDX), is Fe-29.2Mn5.2Si1.3Pd (wt.%) for the fully-compact alloy, and Fe-29.1Mn6.1Si0.7Pd1.6O (wt.%), Fe-29.4Mn5.9Si0.7Pd2.0O (wt.%) and Fe-29.4Mn5.8Si0.5Pd1.3O (wt.%) for the alloys produced with 10, 20 and 40 wt.% NaCl, respectively.

2.2. Immersion tests

Prior to immersion tests, pieces of 9 mm in diameter and thickness of 2.5 mm from the as-sintered porous Fe-30Mn6Si1Pd alloys were immersed in 40 mL of Hank' s balanced salt solution at 37±1 °C for 7 days, 14 days, and 30 days. For comparison purposes, pieces of 3 mm in diameter and 1 mm thickness of the as-cast fully-compact alloy were also immersed in 5 mL of Hank's solution (to maintain the surface-area to solution-volume ratio constant among different samples) for the same periods of time.

The volume of solution was selected to conform with the ASTM-G31-72 norm [24]. After each immersion process, the samples were removed from the Hank's solution, rinsed with alcohol, and dried in air. The microstructure, and the magnetic and mechanical properties were subsequently assessed as a function of immersion time.

2.3. Structural Characterization

Scanning electron microscopy (SEM) observations were done on a Zeiss Merlin microscope equipped with an energy dispersive X-ray (EDX) spectroscopy detector for compositional analyses. X-ray diffraction (XRD) was carried out on a Philips X'Pert

diffractometer using Cu K_α radiation. The measurements were performed in the angular range 2θ = 30–100° with a step size of 0.026°.

2.4. Characterization of mechanical and magnetic properties

Nanoindentation measurements were carried out on the as-cast and post-immersion samples using a UMIS nanoindenter from Fischer-Cripps Laboratories, with a Berkovich pyramidal-shaped diamond indenter. The maximum applied load was 500 mN. The results were averaged over more than 20 indents for each sample to obtain statistically reliable data. The Berkovich hardness (H) and reduced Young's moduli (E_r) were evaluated from the load–displacement curves, at the beginning of the unloading segments, using the method of Oliver and Pharr [25]. Hysteresis loops were recorded at room temperature using a vibrating sample magnetometer (VSM) from MicroSense, with a maximum applied magnetic field of 20 kOe.

2.5. Electrochemical potentiodynamic polarization measurements

The corrosion behavior of the as-cast and as-sintered alloys was evaluated by potentiodynamic polarization tests in a single compartment, double-walled cell with a typical three-electrode configuration (connected to an Autolab PGSTAT302N potentiostat/galvanostat) at 37±1 °C in Hank's solution. A double junction Ag/AgCl with 3 M KCl inner solution and 1 M NaCl outer solution was used as reference electrode, while a Pt spiral was used as counter electrode, respectively. Prior to the measurements, the specimens were immersed in the electrolyte for 1 h to determine the open circuit potential (OCP). Three samples of each composition were measured to ensure good repeatability. The upper and lower potential limits of the linear sweep voltammetry were set at –1000 mV and +1000 mV. The scan rate was 0.5 mV/s. I_{corr} and E_{corr} were calculated by the classical Tafel analysis which is performed by extrapolating the linear portions of a logarithmic current versus potential plot back to their intersection. The value of either the anodic or the cathodic current at the intersection is I_{corr}.

2.6. Cytotoxicity assays

The human osteosarcoma cell line Saos-2 was used to assess the cytotoxicity of both fully-compact and porous alloys. The Saos-2 cell line was routinely maintained in T25 culture flasks, using DMEM high glucose medium supplemented with 10% Fetal Bovine Serum (FBS) (both from Gibco). To perform the cytotoxicity experiments, $1.5x10^5$ cells were seeded into 6-well plates and, once attached to the plate surface, cells were incubated with conditioned medium during 14 days.

To obtain the conditioned medium, alloys were sterilized with dry heat during 3 h at 150 ºC and at least 3 disks from each alloy were individually incubated with 4 mL of DMEM + 10% FBS in 6-well plates at 37 ºC and 5% of CO_2. After 24 h, the conditioned medium, enriched with ions and particles released by the alloys, was pooled, filtered (0.2 µm of diameter from Fisher Scientific) and kept at 4 ºC until its use in cell cultures. Fresh medium was added to the same alloy disks and the collection of conditioned medium was repeated using the same procedure at days 3, 7, 10 and 14 from the start of the incubation.

The Live/Dead viability/cytotoxicity kit (Molecular Probes) was used following the manufacturer's instructions for a qualitative analysis of cell viability at 1 and 14 days of culture in conditioned media. This kit allows for the simultaneous detection of living (green fluorescence) and dead (red fluorescence) cells. Images were captured using an Olympus IX71 inverted fluorescence microscope.

The Alamar blue assay (Invitrogen) was used for a quantitative analysis of cell viability and proliferation. Resazurin, the active compound of Alamar Blue, is only reduced to resorufin (a fluorescent product) by viable cells. To perform these experiments, cells were incubated with each conditioned medium as illustrated in Figure 2. After the corresponding incubation time, the medium was replaced by fresh medium containing 10% of Alamar blue and the cells were incubated for 2 h at 37 ºC protected from light. Then, the medium was collected and the fluorescence intensity was measured with a Cary Eclipse Fluorescence Spectrophotometer.

Results are the average of three independent experiments performed for each alloy and condition. Control cultures with fresh medium were also performed in triplicate. The

ANOVA test for multiple comparisons was used to assess statistical differences in the mean values of living cells cultured in conditioned medium from the different materials at each time point. Data was normalized with control cultures, and significance was considered for $p < 0.05$.

3. Results and discussion

3.1. Microstructure and compositional analyses

3.1.1. Morphology, chemical composition and crystallographic phase composition of the as-prepared alloys

Figure 3 shows top-view SEM micrographs of as-cast fully-compact Fe-30Mn6Si1Pd (panel a), Fe-30Mn6Si1Pd-10%NaCl (panel b), Fe-30Mn6Si1Pd-20%NaCl (panel c) and Fe-30Mn6Si1Pd-40%NaCl (panel d) as-prepared alloys. In the fully-compact Fe-30Mn6Si1Pd alloy, the typical dendritic morphology, together with Pd-rich precipitates [14], can be observed. Such dendritic morphology is not detected in the porous counterparts. In that case, depending on the amount of NaCl, different degrees of porosity, as well as differences in the pore size, are observed. The porosity mainly originates from the decomposition of the porogen NaCl crystals; therefore, larger amounts of NaCl give rise to more porous specimens [26]. Pore size also tends to increase with increasing the amount of NaCl as a result of the larger chances of coalescence between NaCl crystals. Zhang et al. [27] also reported that pore sizes larger than the crystal size could be obtained when employing NH_4HCO_3 as a porogen, when the spacer amount was up to a certain value (20 vol.%). The pore size histograms of the as-prepared porous alloys are shown in the insets of Figure 3. The average pore size values in the alloys with 10, 20 and 40 wt.% of NaCl are 3.7 ± 1.5 μm, 5.7 ± 2.3 μm and 8.6 ± 3.0 μm, while the size of the NaCl powders after ball milling is 4.4 ± 1.9 μm. Hence coalescence and interconnection between neighboring NaCl particles indeed took place for large NaCl contents. It is also worthy to mention that the alloy particles exhibit

intrinsic nanometer-size porosity, independently of the amount of NaCl, as a result of the compaction and sintering process.

The porosity and the density of the sintered alloys is listed in Table 1. As expected, the addition of NaCl significantly increases the porosity of the compacts (i.e. the alloys produced with 10 wt.% of NaCl show a 25.9% of porosity while those produced with 40 wt.% of NaCl resulted in 62.3 % of porosity)

Figure 4 illustrates the XRD patterns of the as-cast fully-compact and as-prepared porous Fe-30Mn6Si1Pd alloys. The as-cast bulk Fe-30Mn6Si1Pd is composed of ε-martensite ($P6_3/mmc$, a = 2.55 Å, c = 4.14 Å) and retained γ-austenite (Fm3m, a = 3.60 Å) phases. Conversely, only γ-austenite (together with minor reflections belonging to oxide formation) can be observed in the XRD patterns of the porous Fe-30Mn6Si1Pd alloys. The structural differences observed among the bulk and porous alloys can be attributed to the technique used to fabricate the alloys rather than to changes in composition. In the fully-compact alloys, the higher cooling rate achieved during suction casting into a refrigerated Cu mould promotes the austenite-to-martensite phase transformation. Nonetheless, the cooling rate was not high enough and retained austenite was kept mixed with the martensite phase. Conversely, the sintered powders were cooled from 900 ºC to room temperature inside a furnace, hence with a much slower cooling, favoring the complete formation of austenite phase.

3.1.2. Morphology, chemical composition and crystallographic phase composition analyses as a function of immersion time

Figure 5 compares the SEM images of the fully-compact and porous alloys after immersion in Hank's solution for 30 days. While in the bulk Fe-30Mn6Si1Pd alloy (panel a) a compact and smooth oxide layer on the outermost surface was previously identified [14], the corrosion products for the porous Fe-30Mn6Si1Pd alloys (panels b, c and d) were coating the Fe-based particles in a non-continuous manner. For the Fe-30Mn6Si1Pd-10%NaCl, the porous structure almost collapsed and considerably smaller voids are observed compared to the as-prepared alloy (i.e., the porous structure is almost lost). Similar morphology can be

observed in the Fe-30Mn6Si1Pd-20%NaCl alloy although, in this case, some of the pores are still visible, although being smaller. On the contrary, the porous structure of the Fe-30Mn6Si1Pd-40%NaCl sample clearly remains after 30-days immersion. To shed light on the degradation mechanisms of these alloys, cross section SEM images after 30 days immersion in Hank's solution are presented in Figure 6 for the as-cast fully-compact and for the porous (20 wt.% NaCl) specimens. While for the fully-compact Fe-30Mn6SiPd alloy a compact 3–5 μm thick oxide layer can be observed at the outermost surface, no evidence of such a compact and continuous oxide-hydroxide layer can be observed anywhere for the Fe-30Mn6Si1Pd-20%NaCl alloy. Remarkably, in this case, the corrosion products were attached at the surface of the alloy particles throughout the thickness (i.e., filling the pores), as the Hank's solution can permeate through the open-cell porous structure of the alloy.

A detailed cross section SEM image of the Fe-30Mn6Si1Pd-20%NaCl alloy after immersion in Hank's solution for 30 days, together with the O, Si, Fe, Mn and Pd element distribution mappings, are shown in Figure 7. The trend is the same for the Fe-30Mn6Si1Pd-10%NaCl and Fe-30Mn6Si1Pd-40%NaCl alloys. The mappings reveal that the pores are filled with corrosion products enriched in Si and O and depleted in Fe and Mn. Si is known to be an element prone to oxidation. In fact, in alkaline solutions, the standard reduction potential (E^o) for the reaction $SiO_3^{2-} + 3H_2O + 4e^- \rightarrow Si + 6OH^-$ is -1.69 V. Meanwhile, the standard potential values for Pd, Fe and Mn are: $E^o_{Pd^{2+}/Pd}$ = 0.95V, $E^o_{Fe^{2+}/Fe}$ = -0.44 V and $E^o_{Mn^{2+}/Mn}$ = -1.18V [28]. Therefore, among all these elements, silicon is the one with the more negative standard potential, thus the easiest to oxidize.

After 30 days of immersion in Hank's solution, severe degradation was observed for the porous samples, especially in the Fe-30Mn6Si1Pd-40%NaCl alloy, so the specimens started to disintegrate. The solution became semi-transparent or even opaque with insoluble orange and dark precipitates. These solid precipitates were produced by chemical reaction with the immersion media and they showed relatively low solubility in the aqueous solution, similar to what has been reported for other Fe-based alloys [27].

In order to gain further insight into the corrosion products formed on the surface of the sample during immersion, XRD was carried out on the Fe-30Mn6Si1Pd-40%NaCl sample after immersion for 7 days, 14 and 30 days (Figure 8). However, the XRD patterns taken at 7

and 14 days do not reveal any additional features compared with the as-prepared sample (Figure 3). This might be attributed to the thin nature of the oxide layer, in good agreement with the on-top SEM observations. XRD could neither capture the pore filling phenomena. This could be due to the limited penetration of X-rays (only a few microns from the surface) or the occurrence of amorphous oxides. A slight increase in the intensity of the oxide peaks is observed after 1 month of immersion in Hank's solution for this sample.

3.2. Magnetic properties

The dependence of the magnetization as a function of applied magnetic field for the four as-prepared alloys at room temperature is shown in Figure 9. Bulk fully-compact Fe-30Mn6Si1Pd alloy shows very low magnetic susceptibility compared to SS316L because of the non-magnetic nature of the γ-austenite (actually the Fe-35Mn alloy has been reported to be antiferromagnetic) [29]. Remarkably, the saturation magnetization of the non-porous Fe-30Mn6Si1Pd (0.4 emu/g) is significantly lower than that of pure Fe (217.2 emu/g) or Fe-10Mn6Si1Pd (160 emu/g) [14]. However, slightly larger saturation magnetization (up to 13.5 emu/g, i.e., still relatively low) is detected for the alloys prepared by powder metallurgy and NaCl sublimation, probably because of the thin layer of iron oxide (Fe_2O_3) formed surrounding the Fe-30Mn6Si1Pd particles. However, in terms of biocompatibility, γ-Fe_2O_3 is a well-accepted magnetic material for biomedical applications, such as targeted delivery, cell labeling, and its excellent biocompatibility has been confirmed [30].

After immersion in Hank's solution for 30 days, the magnetization of the Fe-30Mn6Si1Pd alloys remain almost unaltered (Figure S1), corroborating that the corrosion products mainly consist of SiO_2 and other non-magnetic oxides and hydroxides.

3.3. Evolution of mechanical properties

The mechanical properties of the as-prepared and immersed alloys were measured by nanoindentation. Nanoindentation is a suitable technique to assess the mechanical properties of bulk materials and films, including porous ones. Indeed, the mechanical properties of

dealloyed nanoporous metals and porous oxide films can be reliably estimated by nanoindentation [24]. However, to avoid the influence of the roughness on the extracted mechanical parameters, the samples were indented in the cross-section after having been polished to mirror-like appearance. Another issue to overcome when indenting porous or rough materials is the scattering in the obtained data. This can be particularly troublesome when the size of the indentation imprint does not embrace a representative region of the specimen (i.e., pore size being much larger than the size of the indentation imprint). In this case, the hardness and Young's modulus can locally vary significantly depending on whether the indentation is performed on top of a pore wall or inside a pore. To minimize this problem, we used a maximum load of 500 mN to embrace the maximum representative surface area, as shown in Figure 10. In addition, several indentations were carried out on different regions of the sample, in order to obtain statistically meaningful data.

The dependences of E_r and H for the Fe-30Mn6Si1Pd-20%NaCl alloy as a function of the immersion time are presented in Figure 11. The as-prepared Fe-30Mn6Si1Pd-20%NaCl alloy exhibits a Young's modulus of 28 GPa, which is close to that of the human bone (from 3-20 GPa). Actually, all the porous Fe-30Mn6Si1Pd samples in the as-produced condition exhibit smaller hardness and Young's modulus than the fully-compact Fe-30Mn6Si1Pd alloy (Figure S3 and Table 2). Both hardness and Young's modulus progressively reduce with the increase of the porosity level because of the decrease of the relative density of the material [21]. Besides porosity, the fully austenite (mechanically softer phase) structure of the porous alloys probably also contributes to the lower hardness of the porous Fe-30Mn6Si1Pd alloys when compared to the fully-compact one, which also contains martensite (mechanically harder phase).

The mechanical properties of the porous compacts can also be discussed using the classical Gibson-Ashby model, where the porosity of the sintered compacts as well as the pore shape play a role on the resulting mechanical properties. According to the Gibson-Ashby model, the Young's modulus of the porous alloys can be calculated as follows [7,31,32]:

$$E_{porous} = C \cdot E_{bulk} \cdot \left(\frac{\varphi_{porous}}{\varphi_{bulk}}\right)^2 \qquad \text{(Eq.1)}$$

where E_{bulk} is the Young's modulus of the bulk, nonporous alloy (i.e., 93 GPa) [14], C is a geometry constant close to 1 and φ_{porous} is the density of the porous alloy calculated using the Archimedes' principle (Table 1). Good agreement is observed between the Young's modulus measured by nanoindentation and the Young's modulus obtained using Eq. 1. (Table 2).

From Figure 11, both hardness and Young's modulus increase for immersion times up to 14 days, and then slightly decrease for long-term immersion in Hank's solution. A similar trend was observed for the alloys with 10 and 40 wt.% of porosity. The increase in hardness and Young's modulus can be attributed to the harder and stiffer nature of the corrosion products filling the holes. However, with prolonged immersion times, these filling oxide materials as well as the alloys themselves, start to lose their integrity, resulting in relatively low Young's modulus. Remarkably, E_r of all the porous alloys reaches values close to 20 GPa after long-term immersion, a value which is close to the Young's modulus of human bones (3–27 GPa), hence favoring good biomechanical compatibility between an eventual implant and the neighboring bone tissue [29].

3.4. Corrosion Behavior and corrosion mechanism

The potentiodynamic polarization curves for the four alloys in Hank's solution are shown in Figure 12. The curves for the porous alloys all display a similar profile. The anodic branch shows an abrupt increase of the current density at -0.6 V once passed the corrosion potential (E_{corr}) an afterwards the current stabilizes. Meanwhile, the fully-compact sample does not show any plateau after crossing E_{corr} and almost immediately undergoes oxidation. In any case, both the corrosion current density (J_{corr}) and E_{corr} are significantly different among samples. J_{corr} is commonly used as a criterion to evaluate the kinetics of a corrosion process as the corrosion rate is normally proportional to J_{corr}. According to Table 3, the order of the corrosion rate is Fe-30Mn6Si1Pd-40%NaCl > Fe-30Mn6Si1Pd-20%NaCl > Fe-30Mn6Si1Pd-10%NaCl > Fe-30Mn6Si1Pd. In addition, the corrosion potential (E_{corr}) follows the same trend, indicating that corrosion initiates at a more cathodic potential as porosity increases. Accordingly, the corrosion resistance (R_p) values diminish. These

observations are commonly noted in open-cell porous materials where higher degree of porosity results in larger surface areas exposed to the corrosive media (Hank's solution) [27]. Note that the surface of the non-porous alloy was mechanically polished to mirror-like finish for the electrochemical corrosion experiments. However, the porous specimens were not polished as this would result in a partial collapse of the pores, hence, significantly altering their surface morphology. Since the chemical composition was highly homogeneous across samples' surface, differences in the corrosion behavior can be directly attributed to the occurrence of porosity. Pores cause a remarkable increase in the surface area of the specimens and, at the same time, act as defects, thereby making the specimens more prone to corrosion. The main degradation mechanism for both, bulk and porous, Fe-30Mn6Si1Pd alloys is based on the electrochemical reaction of the material in contact with the media to produce oxides, hydroxides, hydrogen gas, or other compounds, as it has been reported by many authors [4,15,27]. Our results indicate that the formation of Si-rich oxides takes place indeed in the porous alloys. In the fully-compact specimen, Ca and P elements could be detected by EDX at the end of the electrochemical polarization tests. The formation of a calcium/phosphorous layer is considered as the last step in the cascade of reactions affecting metallic alloys exposed to simulated body fluids [15]. However, these elements were not detected in its porous counterparts, likely as a result of a faster kinetics of ion release, which would preclude the formation of a stable Ca,P-containing layer.

3.5. Cytotoxicity

Cytotoxicity can promote different cell responses such as necrosis, apoptosis or reduced cell proliferation. The analysis of cell viability only distinguishes between living and dead cells, whereas the analysis of cell proliferation provides additional information on the cell cycle progression, which can be slowed down or even arrested in living cells suffering toxic effects. Thus, for a global measurement of the potential cytotoxicity of bulk and porous alloys, both cell viability and proliferation were assessed at different time-points. The high corrosion and degradation rate of the porous disks surface caused thin layers of material to quickly detach from the alloys surface, preventing cell adhesion during the first 24 h of culture (Figure S4)

and precluding the assessment of cytotoxicity in cells growing directly on the alloys. For this reason, conditioned medium was used to perform the biological experiments. The higher the porosity of the alloys, the larger the loss of integrity of the alloy surface, which is in agreement with the immersion test results.

Qualitative analyses of cell viability showed that on day 1 most of the cells were alive, but the cell density in cultures incubated with conditioned medium was slightly lower than in control cultures, regardless of the type of alloy (Figure S5). On day 14, cell density decreased in cultures containing conditioned media from all porous alloys compared with those containing conditioned media from the bulk alloy and control cultures (Figure 13). Quantitative analysis confirmed that there were no significant differences in cell viability between the control and bulk alloy cultures, but the percentage of living cells significantly decreased in all porous alloy cultures (Figure 14a). In cultures incubated with conditioned medium from the Fe-30Mn6Si1Pd-10%NaCl and Fe-30Mn6Si1Pd-20%NaCl alloys the decrease in cell viability was similar and significantly lower than the decrease observed in 40% porous alloy cultures (Figure 14a), where only a few living cells remained attached to the plate surface (Figure 13). Nevertheless, the reduction in cell viability in cultures containing the Fe-30Mn6Si1Pd-10%NaCl and Fe-30Mn6Si1Pd-20%NaCl alloys conditioned medium, although statistically significant when compared to control and bulk alloy cultures, was below 30%, satisfying the ISO 10993-5 standard, which considers a cytotoxic effect when the cell viability is lower than 70%.

Proliferation analyses (Figure 14b) demonstrated no significant differences between control and bulk alloy cultures, which formed a confluent monolayer on day 7 that was maintained on day 10. Cells cultured in conditioned medium from the Fe-30Mn6Si1Pd-10%NaCl and Fe-30Mn6Si1Pd-20%NaCl alloys also proliferated until day 7, but from then a reduction in the number of cells was observed until day 10. In contrast, cell proliferation in the 40% porous alloy cultures was only observed between days 1 and 3, at very low levels, and from day 3 a progressive reduction in cell number was observed, indicating a high toxicity of this alloy.

In summary, the bulk alloy is not cytotoxic, neither in terms of cell viability nor of proliferation, whereas the Fe-30Mn6Si1Pd-40%NaCl clearly has a cytotoxic effect. This

toxicity is probably due to the faster and higher ion release from the porous alloys compared with the bulk one, as shown by the results from the immersion tests and the corrosion characterization.

4. Conclusions

1. While porous Fe-30Mn6Si1Pd alloys are composed by γ-austenite, the bulk fully-compact Fe-30Mn6Si1Pd alloy mainly consists of ε-martensite and γ-austenite Fe-rich phases. Minor contents of Pd-rich precipitates are observed in both bulk and porous materials.
2. The porosity of the Fe-30Mn6Si1Pd alloys increases with increasing the NaCl volume fraction. By increasing the amount of NaCl from 10 to 40 wt.%, the Young's modulus decreases from 55 GPa to 7 GPa, hence matching the Young's modulus of human bone.
3. Corrosion resistance is inversely proportional to porosity. E_{corr} shifts to more cathodic values and j_{corr} raises as the porosity of the material increases.
4. Hardness and Young's modulus tend to increase for immersion periods up to 14 days probably because of the formation of mechanically-hard corrosion products (i.e. oxides and hydroxides) filling the pores. However, for longer immersion times, their structural coherence declines, resulting in lower Young's modulus, again not far from that of the human bone.
5. All the investigated alloys are virtually non-magnetic. No significant variations in the overall magnetic properties are observed for immersion times up to 30 days.
6. Bulk alloy is not cytotoxic and does interfere neither with cell viability nor proliferation. Fe-30Mn6Si1Pd-10%NaCl and Fe-30Mn6Si1Pd-20%NaCl, according to the ISO 10993-5, cannot be considered cytotoxic. However, the Fe-30Mn6Si1Pd-40%NaCl alloy has a strong cytotoxic effect from day 3 of cell culture. Hence, the faster and higher corrosion and ion release from highly porous specimens compromise their biocompatibility.

Acknowledgments

This work has been partially funded by the 2014-SGR-1015 and the 2014-SGR-524 projects from the Generalitat de Catalunya, and the MAT2014-57960-C3-1-R (co-financed by the *Fondo Europeo de Desarrollo Regional*, FEDER), and the MAT2014-57960-C3-3-R projects from the Spanish *Ministerio de Economía y Competitividad* (MINECO). JF acknowledges the Juan de la Cierva Fellowship from MINECO (IJCI-2015-27030) and EP is grateful to MINECO for the "Ramon y Cajal" contract (RYC-2012-10839).

References

[1] S.V. Muley, A.N. Vidvans, G.P. Chaudhari, S. Udainiya, An assessment of ultra fine grained 316L stainless steel for implant applications, Acta Biomater. 30 (2016) 408-419.

[2] N. Jha, D.P. Mondal, J.D. Majumdar, A. Badkul, A.K. Jha, A.K. Khare, Highly porous open cell Ti-foam using NaCl as temporary space holder through powder metallurgy route, Mater. Design 47 (2013) 810-819.

[3] E. Zhang, C. Liu, A new antibacterial Co-Cr-Mo-Cu alloy: Preparation, biocorrosion, mechanical and antibacterial property, Mater. Sci. Eng. C 69 (2016) 134-143.

[4] Y.F. Zheng, X.N. Gu, F. Witte, Biodegradable metals, Mater. Sci. Eng. R 77 (2014) 1-34.

[5] Y.W. Song, D.Y. Shan, E.H. Han, Electrodeposition of hydroxyapatite coating on AZ91D magnesium alloy for biomaterial application, Mater. Lett. 62 (2008) 3276-3279.

[6] M. Schinhammer, A.C. Hanzi, J.F. Loffler, P.J. Uggowitzer, Design strategy for biodegradable Fe-based alloys for medical applications, Acta Biomater. 6 (2010) 1705-1713.

[7] E. Pellicer, S. Gonzalez, A. Blanquer, S. Suriñach, M.D. Baró, L. Barrios, et al., On the biodegradability, mechanical behavior, and cytocompatibility of amorphous $Mg_{72}Zn_{23}Ca_5$ and crystalline $Mg_{70}Zn_{23}Ca_5Pd_2$ alloys as temporary implant materials, J. Biomed. Mater. Res. A 101 (2013) 502-517.

[8] P-C. Wong, P-H. Tsai, T-H. Li, C-K Cheng, J.S.C. Jang, J.C. Huang, Degradation behavior and mechanical strength of Mg-Zn-Ca bulk metallic glass composites with Ti particles as biodegradable materials, Journal of Alloys and Compounds, J. Alloy Compd. 699 (2017) 914-920.

[9] Z. Li, M. Chen, W. Li, H. Zheng, C. You, D. Liu, F. Jin, The synergistic effect of trace Sr and Zr on the microstructure and properties of a biodegradable Mg-Zn-Zr-Sr alloy, J. Alloy Compd. 702 (2017) 290-302.

[10] F. Moszner, A.S. Sologubenko, M. Schinhammer, C. Lerchbacher, A.C. Hanzi, H. Leitner, et al., Precipitation hardening of biodegradable Fe–Mn–Pd alloys, Acta Mater. 59 (2011) 981-991.

[11] M. Schinhammer, C.M. Pecnik, F. Rechberger, A.C. Hanzi, J.F. Loffler, P.J. Uggowitzer, Recrystallization behavior, microstructure evolution and mechanical properties of biodegradable Fe–Mn–C(–Pd) TWIP alloys, Acta Mater. 60 (2012) 2746-2756.

[12] T. Kraus, F. Moszner, S. Fischerauer, M. Fiedler, E. Martinelli, J. Eichler, et al., Biodegradable Fe-based alloys for use in osteosynthesis: outcome of an in vivo study after 52 weeks, Acta Biomater. 10 (2014) 3346-3353.

[13] F. Moszner, S.S.A. Gerstl, P.J. Uggowitzer, J.F. Loffler, Atomic-scale characterization of prior austenite grain boundaries in Fe-Mn-based maraging steel using site-specific atom probe tomography, Acta Mater. 73 (2014) 215-226.

[14] Y.P. Feng, A. Blanquer, J. Fornell, H.Y. Zhang, P. Solsona, M.D. Baró, et al., Novel Fe-Mn-Si-Pd alloys: insights into mechanical, magnetic, corrosion resistance and biocompatibility performances, J. Mater. Chem. B 4 (2016) 6402-6412.

[15] H. Hermawan, A. Purnama, D. Dube, J. Couet, D. Mantovani, Fe-Mn alloys for metallic biodegradable stents: degradation and cell viability studies, Acta Biomater. 6 (2010) 1852-1860.

[16] H. Hermawan, H. Alamdari, D. Mantovani, D. Dube, Iron-manganese: new class of metallic degradable biomaterials prepared by powder metallurgy, Powder Metall. 51 (2008) 38-45.

[17] B. Liu, Y.F. Zheng, L.Q. Ruan, In vitro investigation of Fe30Mn6Si shape memory alloy as potential biodegradable metallic material, Mater. Lett. 65 (2011) 540-543.

[18] H. Hermawan, D. Dube, D. Mantovani, Degradable metallic biomaterials: design and development of Fe-Mn alloys for stents, J. Biomed. Mater. Res. A 93 (2010) 1-11.

[19] Z.G. Xu, M.A. Hodgson, P. Cao, A comparative study of powder metallurgical (PM) and wrought Fe-Mn-Si alloys, Mater. Sci. Eng. A 630 (2015) 116-124.

[20] X.N. Gu, Y.F. Zheng, S.P. Zhong, T.F. Xi, J.Q. Wang, W.H. Wang, Corrosion of, and cellular responses to Mg-Zn-Ca bulk metallic glasses, Biomaterials 31 (2010) 1093-1103.

[21] L.J. Gibson, M.F. Ashby, Cellular solids: structure and properties, 2nd ed., Cambridge University Press, 1999.

[22] Z. Xu, M.A. Hodgson, P. Cao, Weight loss behavior of a vacuum sintered powder metallurgical Fe-Mn-Si alloy, J. Mat. Res. 32 (2017)644-655.

[23] A. Šalak, M. Selecka, R. Bureš, Manganese in ferrous powder metallurgy, Powder Metall. Prog. 1 (2001) 41-58.

[24] ASTM Standard G31-72, Standard practice for laboratory immersion corrosion testing of metals, ASTM Standards, Philadelphia, PA, USA, 2004.

[25] W.C. Oliver, G.M. Pharr, An improved technique for determining hardness and elastic-modulus using load and displacement sensing indentation experiments, J. Mater. Res. 7 (1992) 1564-1583.

[26] J. Capek, D. Vojtech, A. Oborna, Microstructural and mechanical properties of biodegradable iron foam prepared by powder metallurgy, Mater. Design 83 (2015) 468-482.

[27] Q. Zhang, P. Cao, Degradable porous Fe-35wt.%Mn produced via powder sintering from NH_4HCO_3 porogen, Mater. Chem. Phys. 163 (2015) 394-401.

[28] W.M. Haynes, Handbook of chemistry and physics, 94th ed., CRC Press, 2013.

[29] H. Hermawan, D. Mantovani, Process of prototyping coronary stents from biodegradable Fe-Mn alloys, Acta Biomater. 9 (2013) 8585-8592.

[30] T.R. Pisanic Ⅱ, J.D. Blackwell, V.I. Shubayev, R.R. Finones, S. Jin, Nanotoxicity of iron oxide nanoparticle internalization in growing neurons, Biomaterials 28 (2007) 2572-2581.

[31] L.J. Gibson, M.F. Ashby, Cellular Solids: Structure and Properties, 2nd ed. (Cambridge University Press, Cambridge, 1997).

[32] D.T. Queheillalt, Y. Katsumura, H.D.G. Wadley, Synthesis of stochastic open cell Ni-based foams, Scripta Mater. 50 (2004) 313-317.

Figure Captions:

Fig. 1: Image of the (a) porous Fe-30Mn6Si1Pd-40%NaCl alloy obtained by press and sinter process and (b) bulk fully-compact Fe-30Mn6Si1Pd alloy produced by arc melting and subsequent suction mould casting.

Fig. 2: Diagram representing how the conditioned media is obtained and the procedure followed for the Alamar Blue (at days 1, 3, 7 and 10) and the Live/Dead (at days 1 and 14) assays. At day 1, Alamar blue and Live/Dead assays were independently performed. CM: conditioned medium.

Fig. 3: SEM images of (a) as-cast fully-compact Fe-30Mn6Si1Pd, (b) Fe-30Mn6Si1Pd-10%NaCl, (c) Fe-30Mn6Si1Pd-20%NaCl and (d) Fe-30Mn6Si1Pd-40%NaCl porous as-prepared alloys. The insets show the pore size distribution for the sintered alloys.

Fig. 4: XRD patterns of as-cast Fe-30Mn6Si1Pd, Fe-30Mn6Si1Pd-10%NaCl, Fe-30Mn6Si1Pd-20%NaCl and Fe-30Mn6Si1Pd-40%NaCl as-prepared alloys.

Fig. 5: SEM images of (a) Fe-30Mn6Si1Pd, (b) Fe-30Mn6Si1Pd-10%NaCl, (c) Fe-30Mn6Si1Pd-20%NaCl and (d) Fe-30Mn6Si1Pd-40%NaCl after 30 days of immersion in Hank's solution.

Fig. 6: Cross section SEM images after 30 days immersion in Hank's solution of (a) Fe-30Mn6SiPd and (b) Fe-30Mn6SiPd alloys-20%NaCl.

Fig. 7: Cross section SEM images of Fe-30Mn6Si1Pd-20%NaCl after immersion in Hank's solution for 30 days together with the element distributions of O, Si, Fe, Mn and Pd.

Fig. 8: XRD patterns of Fe-30Mn6Si1Pd-40%NaCl as a function of immersion time in Hank's solution.

Fig. 9: Dependence of the magnetization as a function of applied magnetic field for as-cast Fe-30Mn6Si1Pd fully-compact alloy, Fe-30Mn6Si1Pd-10%NaCl, Fe-30Mn6Si1Pd-20%NaCl and Fe-30Mn6Si1Pd-40%NaCl porous as-prepared alloys.

Fig. 10: SEM image of an indent obtained after applying a maximum force of 500 mN in the Fe-30Mn6Si1Pd-20%NaCl after 7 days of immersion in Hank's solution.

Fig. 11: Dependence of the reduced Young's modulus (E_r) and hardness (H) for Fe-30Mn6Si1Pd-20%NaCl as a function of immersion time.

Fig. 12: Potentiodynamic polarization curves for Fe-based alloys in Hank's solution at 37 ^{o}C.

Fig. 13: Living (green) and dead (red) cells after 14 days of culture with conditioned medium. Cell density in bulk alloy and control cultures were higher than in cultures containing conditioned medium from all porous alloys. Only a few cells of the Fe-30Mn6Si1Pd-40%NaCl alloy culture remained attached to the plate surface. Scale bar: 100 µm.

Fig. 14: Cell viability (a) and cell proliferation (b) of Saos-2 cells during 10 days of culture with conditioned media. The percentage of living cells was normalized with control cultures. Arbitrary units (a.u.) were used for cell proliferation. Data are the average of three independent experiments. Significance is represented using an alphabetical superscript system on top of the columns. Letters shared in common among the materials at each time point indicate no significant differences whereas different letters indicate statistically significant differences ($p<0.05$). CC: control cultures.

Table 1: % of porosity and density measured using the Archimedes' principle for the alloys produced with 10, 20 and 40 wt.% of NaCl.

Table 2: Young's modulus calculated by nanoindentation at a maximum applied load of 500 mN and Young's modulus calculated using the Gibson-Ashby model for the alloys produced with 10,20 and 40 wt.% of NaCl.

Table 3: Electrochemical data calculated from the potentiodynamic polarization corrosion tests.

Fig. S1: XRD of the Fe-Mn-Si-Pd powders after 1, 3 and 15 hours of milling.

Fig. S2: Dependence of the magnetization as a function of applied magnetic field for fully-compact, as-cast Fe-30Mn6Si1Pd and porous Fe-30Mn6Si1Pd-10%NaCl, Fe-30Mn6Si1Pd-20%NaCl and Fe-30Mn6Si1Pd-40%NaCl alloys after immersion in Hank's solution for 30 days.

Fig. S3: Reduced Young's modulus (E_r) and hardness (H) for as-prepared Fe-30Mn6Si1Pd, Fe-30Mn6Si1Pd-10%NaCl, Fe-30Mn6Si1Pd-20%NaCl and Fe-30Mn6Si1Pd-40%NaCl before and after immersion in Hank's solution for 30 days.

Fig. S4: Alloy surface degradation 24 h after cell seeding: (a) macroscopic view of Fe-30Mn6Si1Pd-40%NaCl alloy degradation (b) debris released from Fe-30Mn6Si1Pd-10%NaCl alloy under an inverted microscope. Scale bar: 100 µm. The inset in (a) shows the formation of an heterogeneous corrosion layer on the alloy surface.

Fig. S5: Living (green) and dead (red) cells after 24 h of cell culture with conditioned medium. A confluent cell monolayer can be seen in control culture whereas cultures

incubated with conditioned medium formed subconfluent monolayers. Images were obtained under a flourescence microscope. Scale bar: 100 µm.

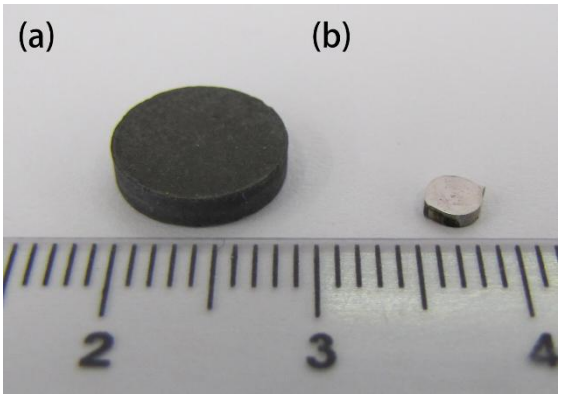

Fig. 1: Image of the (a) porous Fe-30Mn6Si1Pd-40%NaCl alloy obtained by press and sinter process and (b) bulk fully-compact Fe-30Mn6Si1Pd alloy produced by arc melting and subsequent suction mould casting.

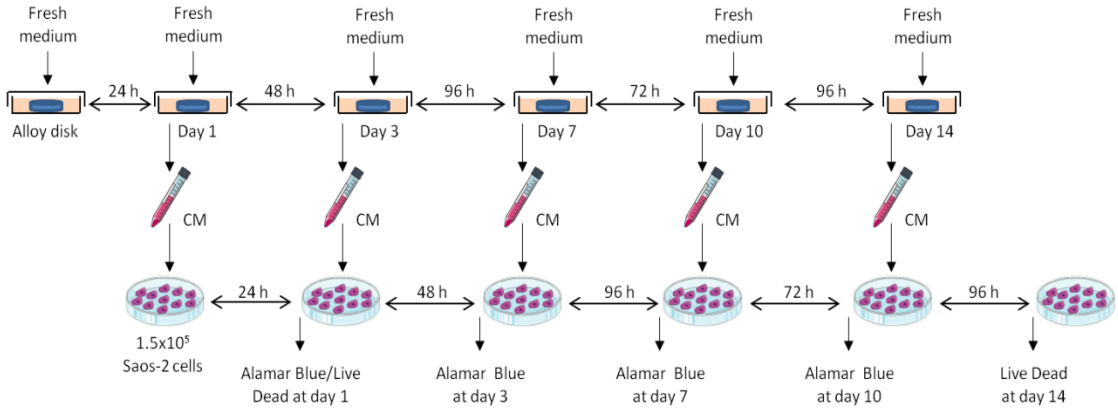

Fig. 2: Diagram representing how the conditioned media is obtained and the procedure followed for the Alamar Blue (at days 1, 3, 7 and 10) and the Live/Dead (at days 1 and 14) assays. At day 1, Alamar blue and Live/Dead assays were independently performed. CM: conditioned medium.

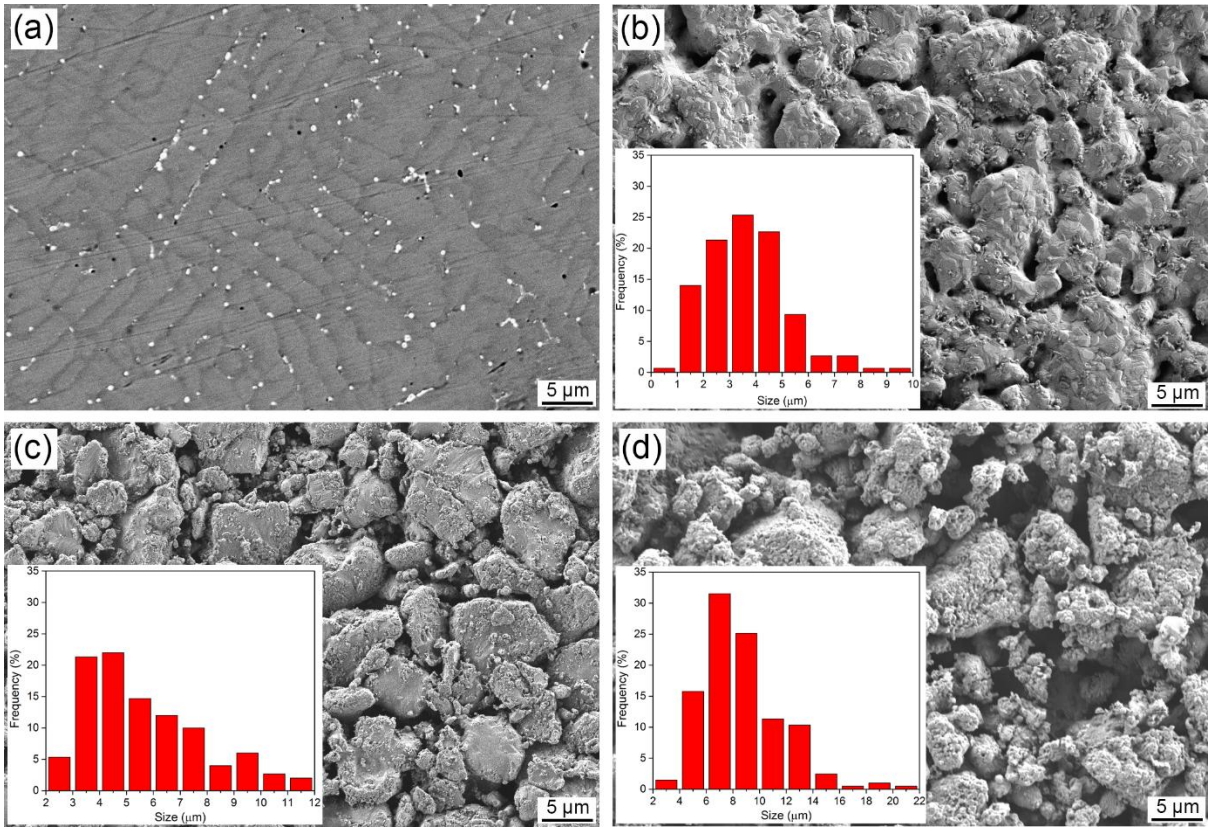

Fig. 3: SEM images of (a) as-cast fully-compact Fe-30Mn6Si1Pd, (b) Fe-30Mn6Si1Pd-10%NaCl, (c) Fe-30Mn6Si1Pd-20%NaCl and (d) Fe-30Mn6Si1Pd-40%NaCl porous as-prepared alloys. The insets show the pore size distribution for the sintered alloys.

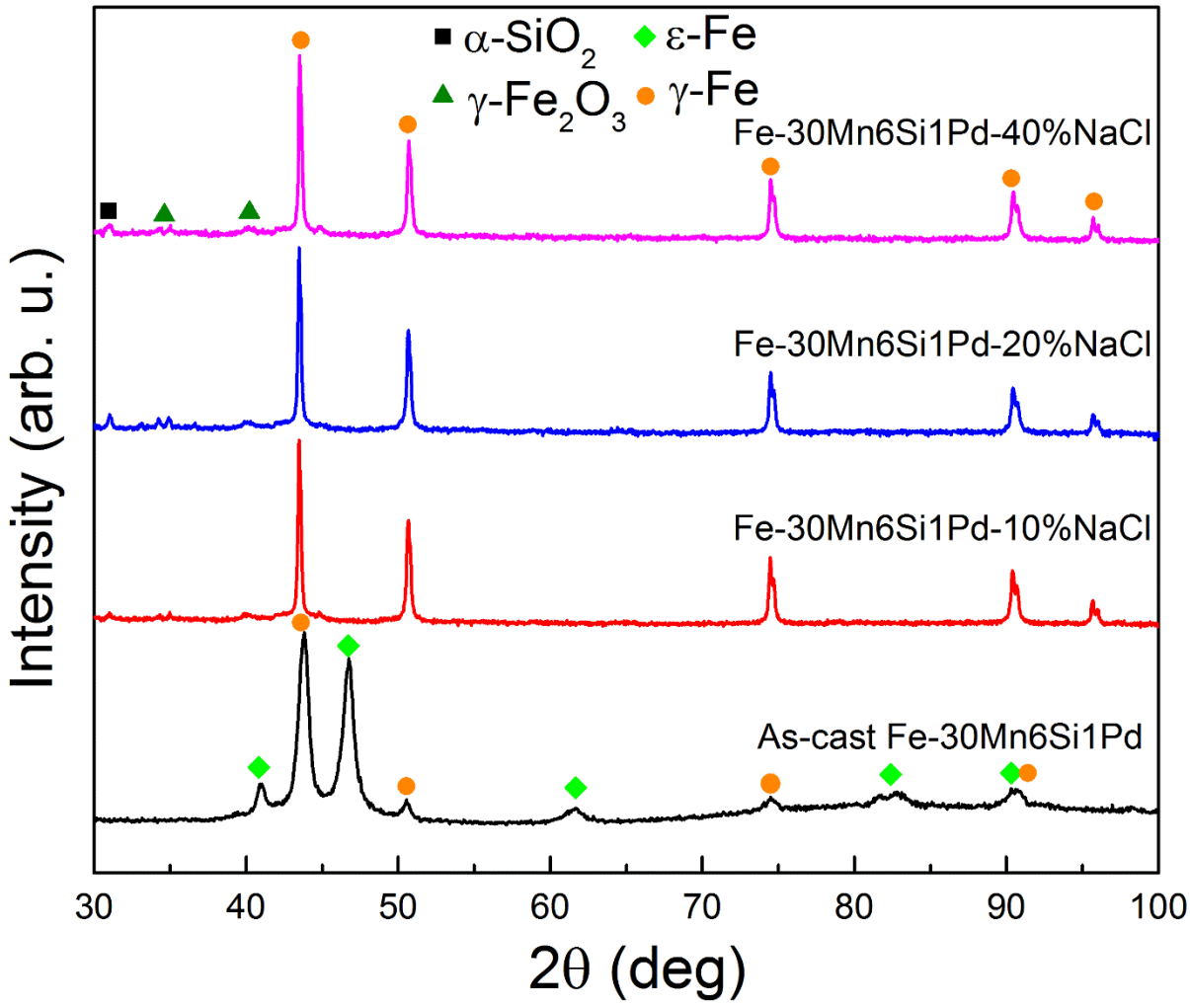

Fig. 4: XRD patterns of as-cast Fe-30Mn6Si1Pd, Fe-30Mn6Si1Pd-10%NaCl, Fe-30Mn6Si1Pd-20%NaCl and Fe-30Mn6Si1Pd-40%NaCl as-prepared alloys.

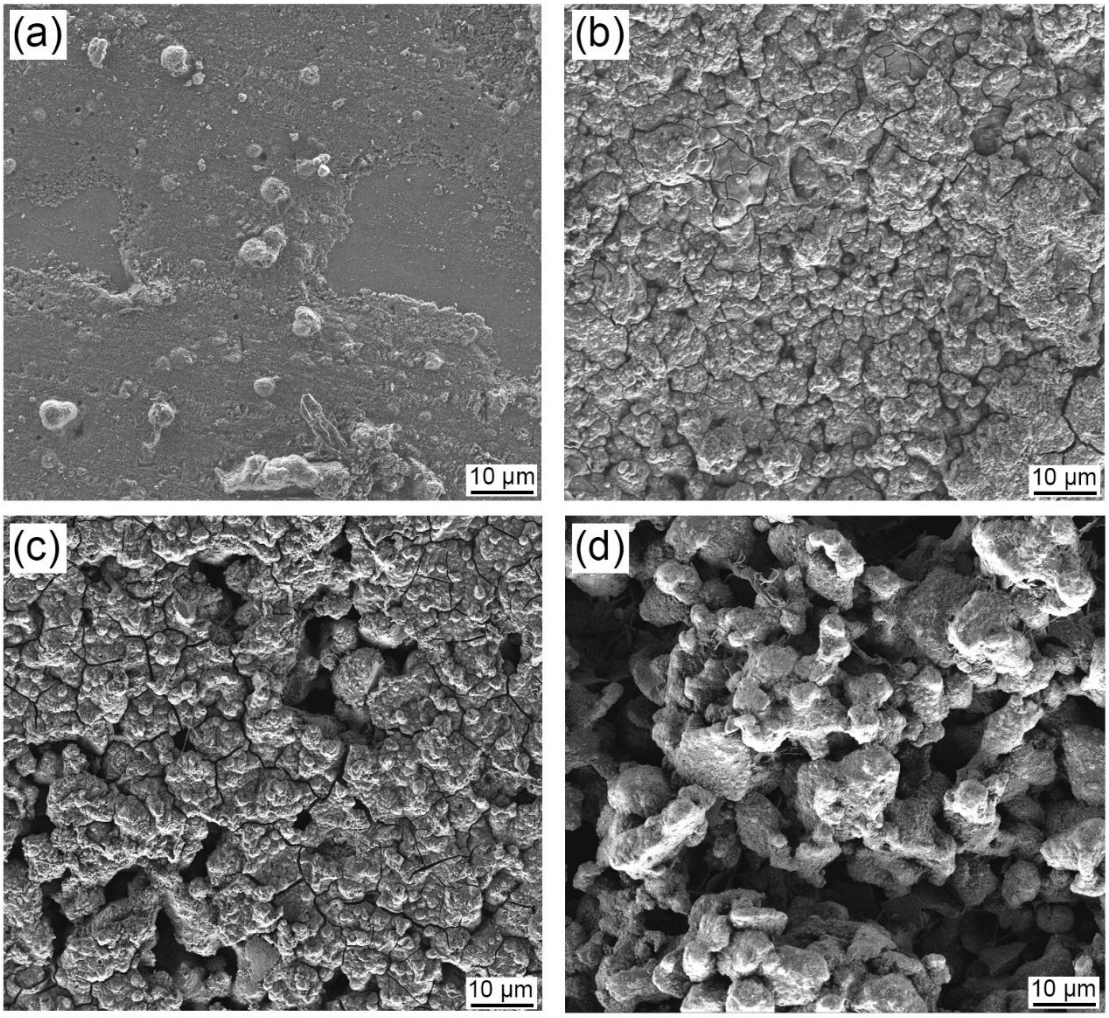

Fig. 5: SEM images of (a) Fe-30Mn6Si1Pd, (b) Fe-30Mn6Si1Pd-10%NaCl, (c) Fe-30Mn6Si1Pd-20%NaCl and (d) Fe-30Mn6Si1Pd-40%NaCl after 30 days of immersion in Hank's solution.

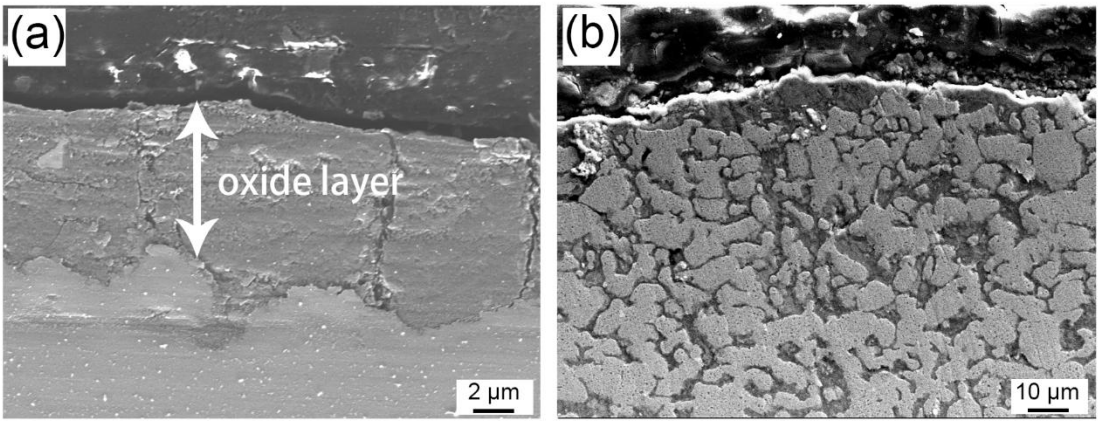

Fig. 6: Cross section SEM images after 30 days immersion in Hank's solution of (a) Fe-30Mn6SiPd and (b) Fe-30Mn6SiPd alloys-20%NaCl.

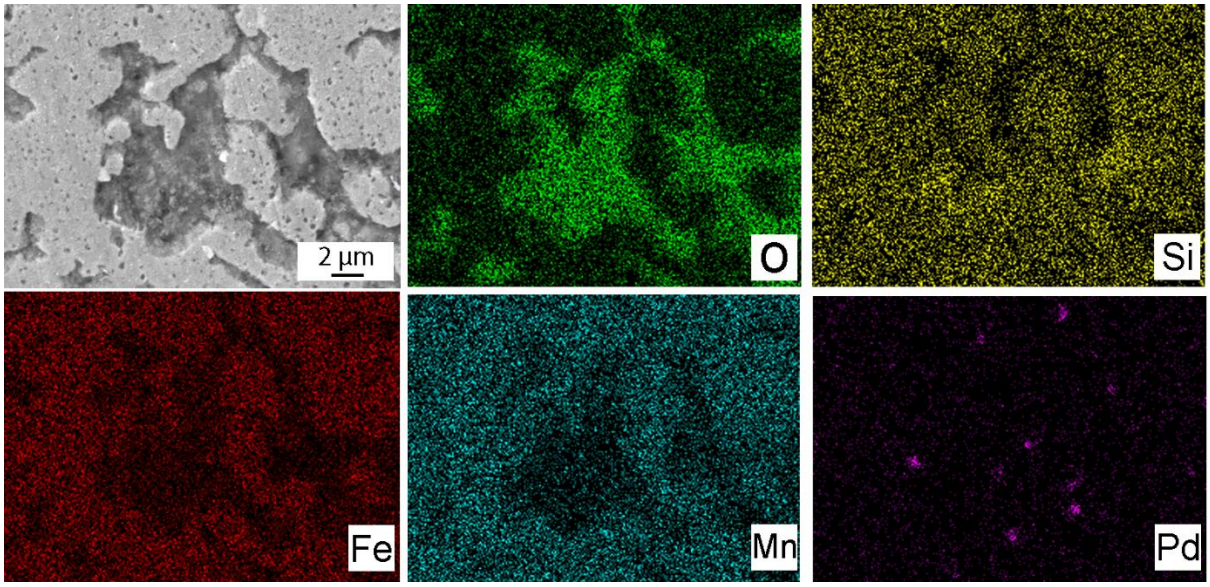

Fig. 7: Cross section SEM images of Fe-30Mn6Si1Pd-20%NaCl after immersion in Hank's solution for 30 days together with the element distributions of O, Si, Fe, Mn and Pd.

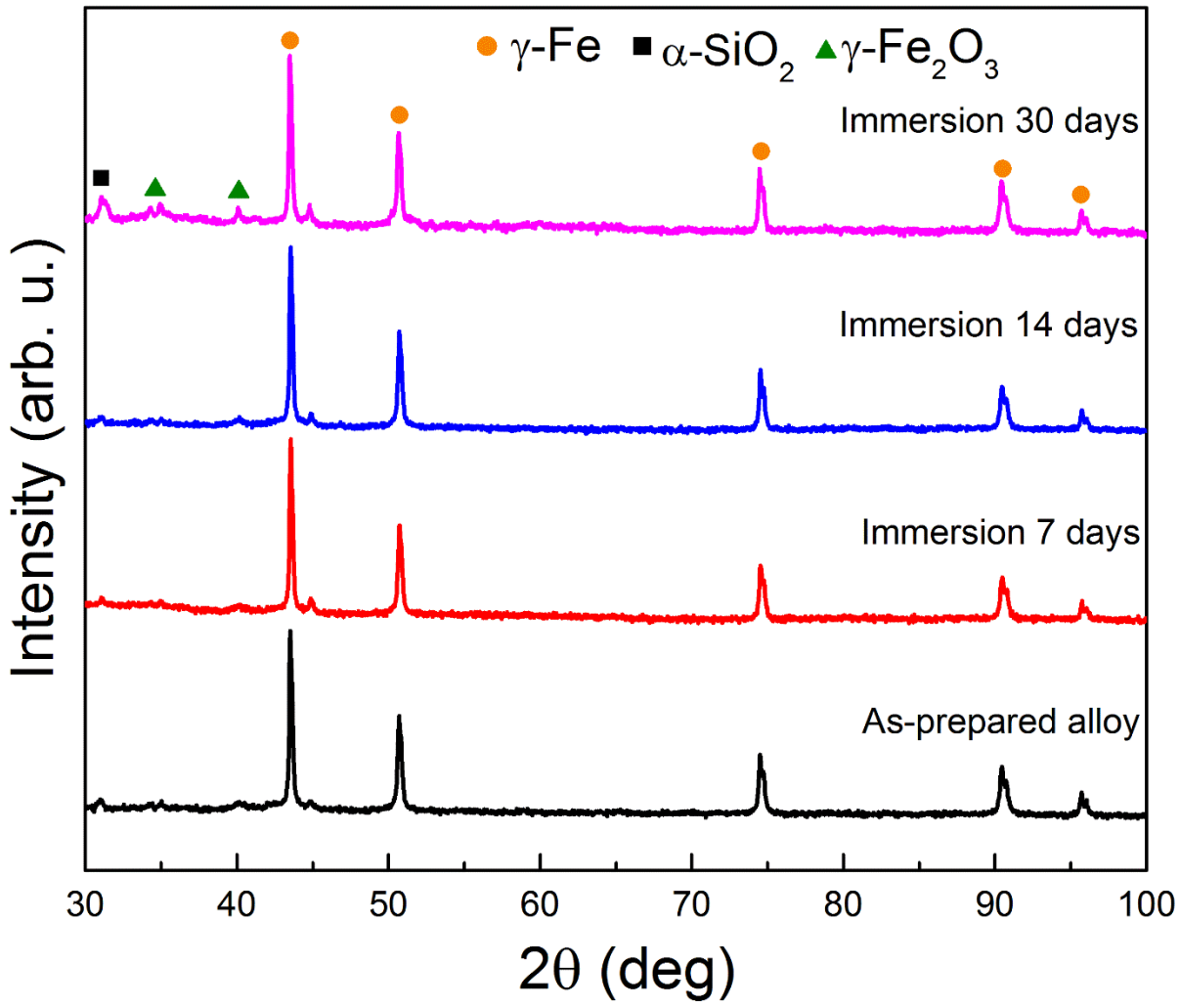

Fig. 8: XRD patterns of Fe-30Mn6Si1Pd-40%NaCl as a function of immersion time in Hank's solution.

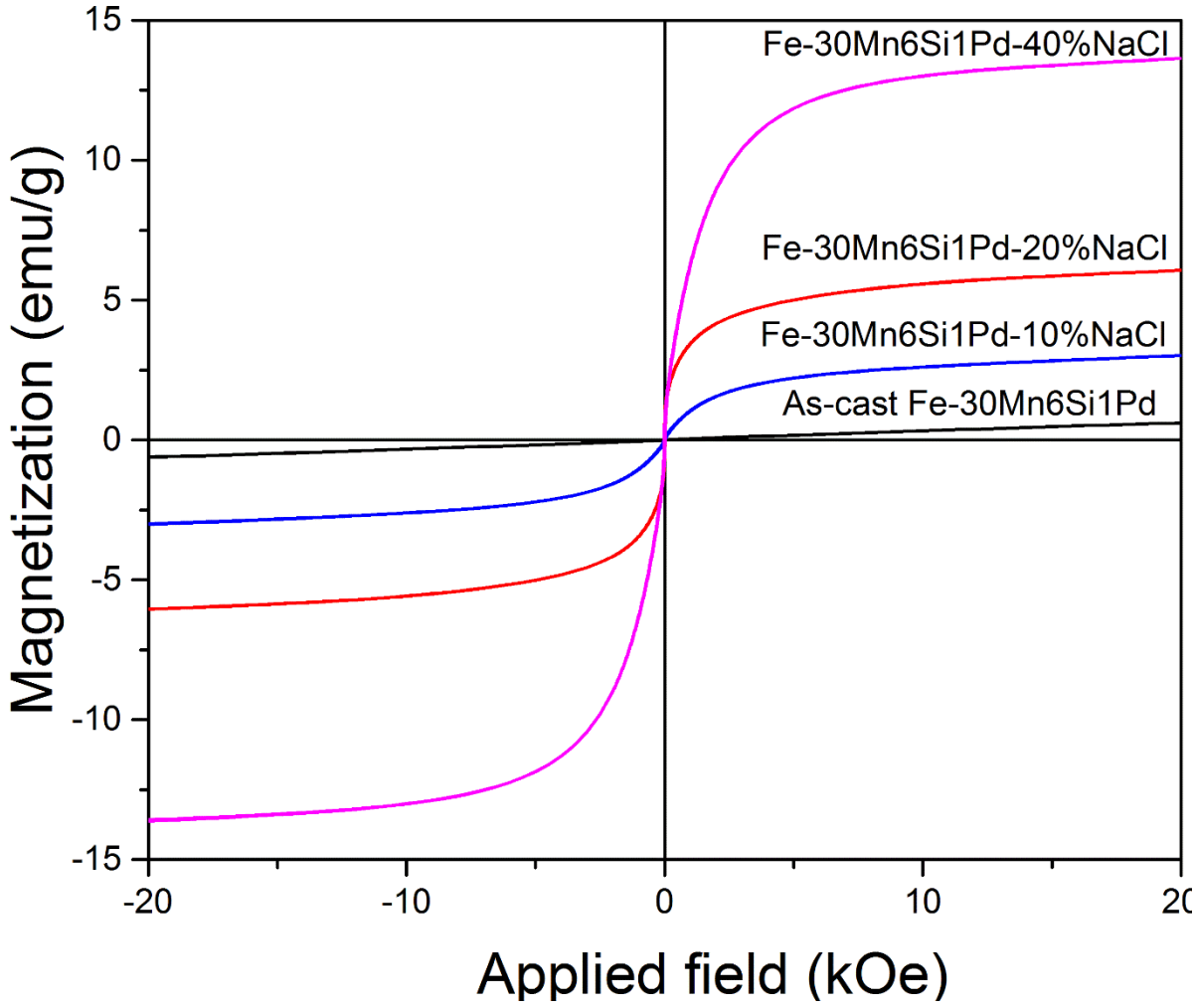

Fig. 9: Dependence of the magnetization as a function of applied magnetic field for as-cast Fe-30Mn6Si1Pd fully-compact alloy, Fe-30Mn6Si1Pd-10%NaCl, Fe-30Mn6Si1Pd-20%NaCl and Fe-30Mn6Si1Pd-40%NaCl porous as-prepared alloys.

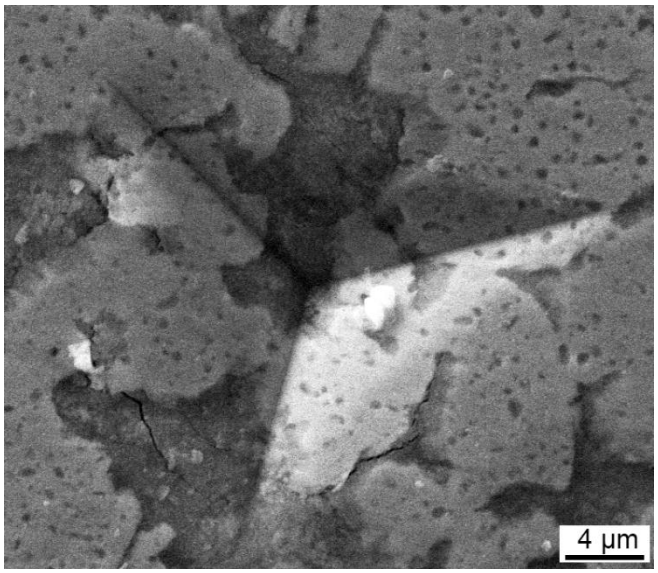

Fig. 10: SEM image of an indent obtained after applying a maximum force of 500 mN in the Fe-30Mn6Si1Pd-20%NaCl after 7 days of immersion in Hank's solution.

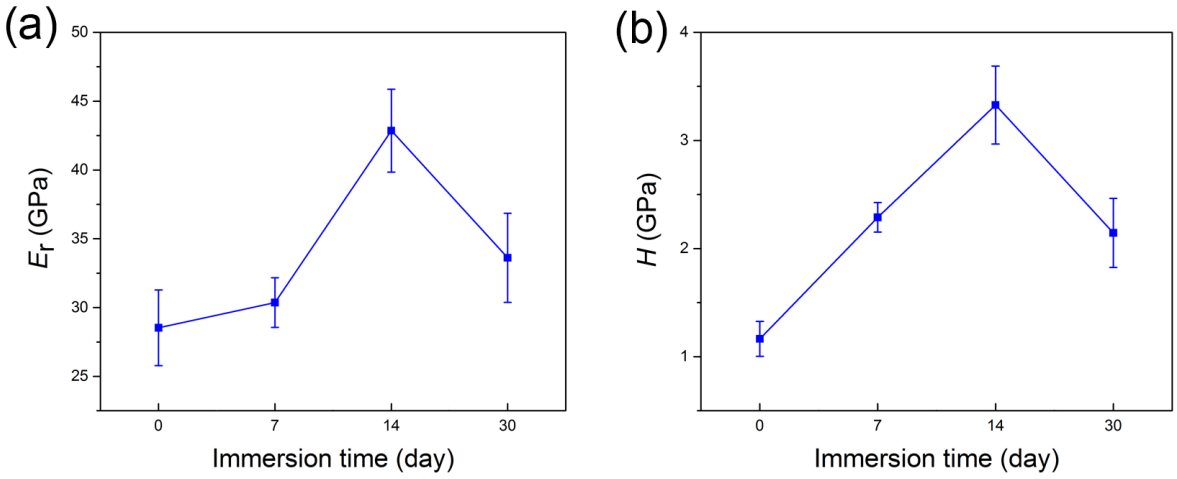

Fig. 11: Dependence of the reduced Young's modulus (E_r) and hardness (H) for Fe-30Mn6Si1Pd-20%NaCl as a function of immersion time.

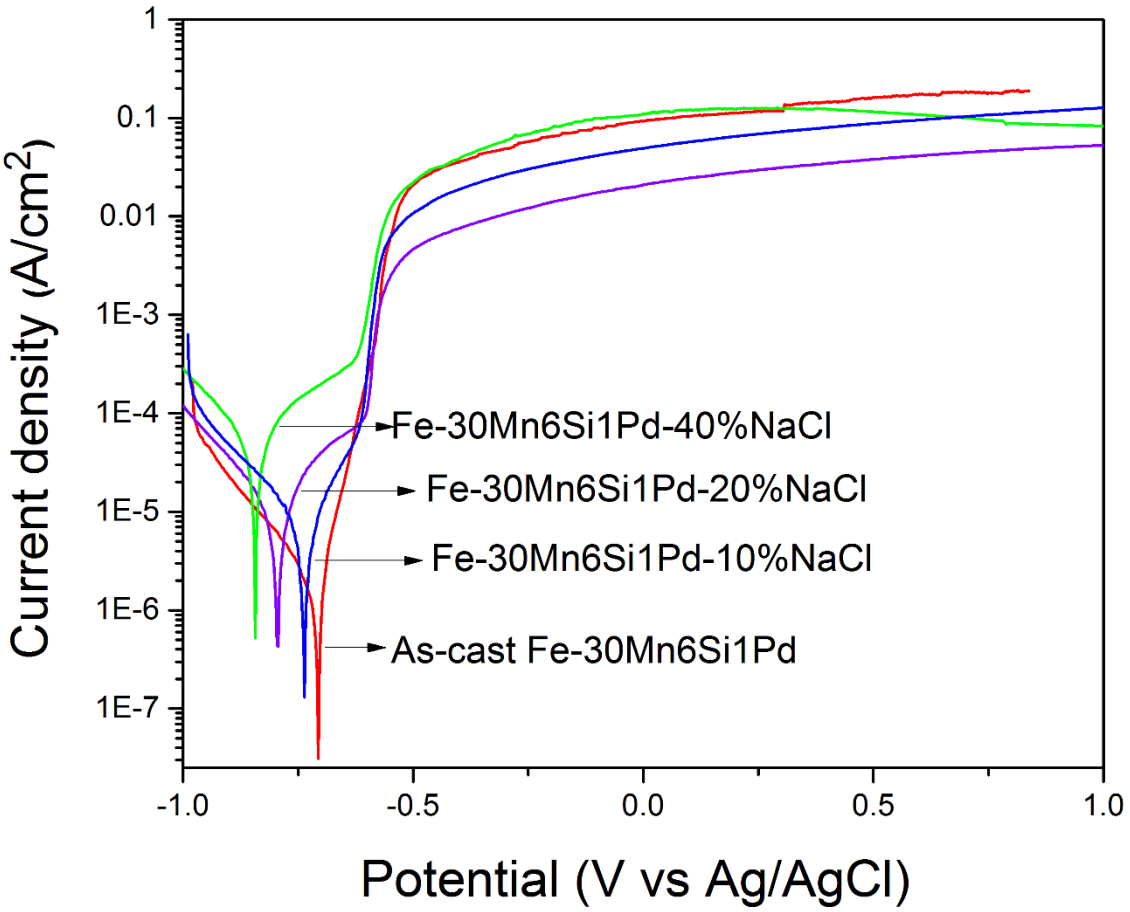

Fig. 12: Potentiodynamic polarization curves for Fe-based alloys in Hank's solution at 37 ^{o}C.

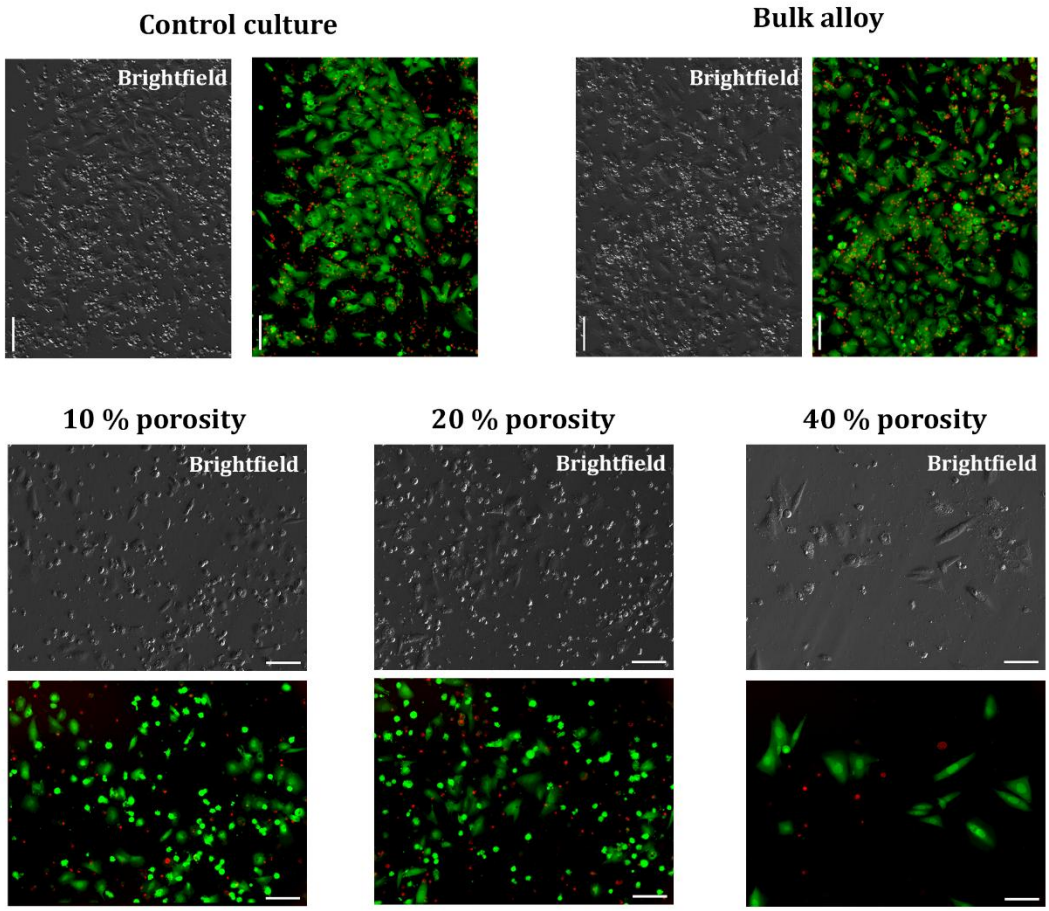

Fig. 13: Living (green) and dead (red) cells after 14 days of culture with conditioned medium. Cell density in bulk alloy and control cultures were higher than in cultures containing conditioned medium from all porous alloys. Only a few cells of the Fe-30Mn6Si1Pd-40%NaCl alloy culture remained attached to the plate surface. Scale bar: 100 µm.

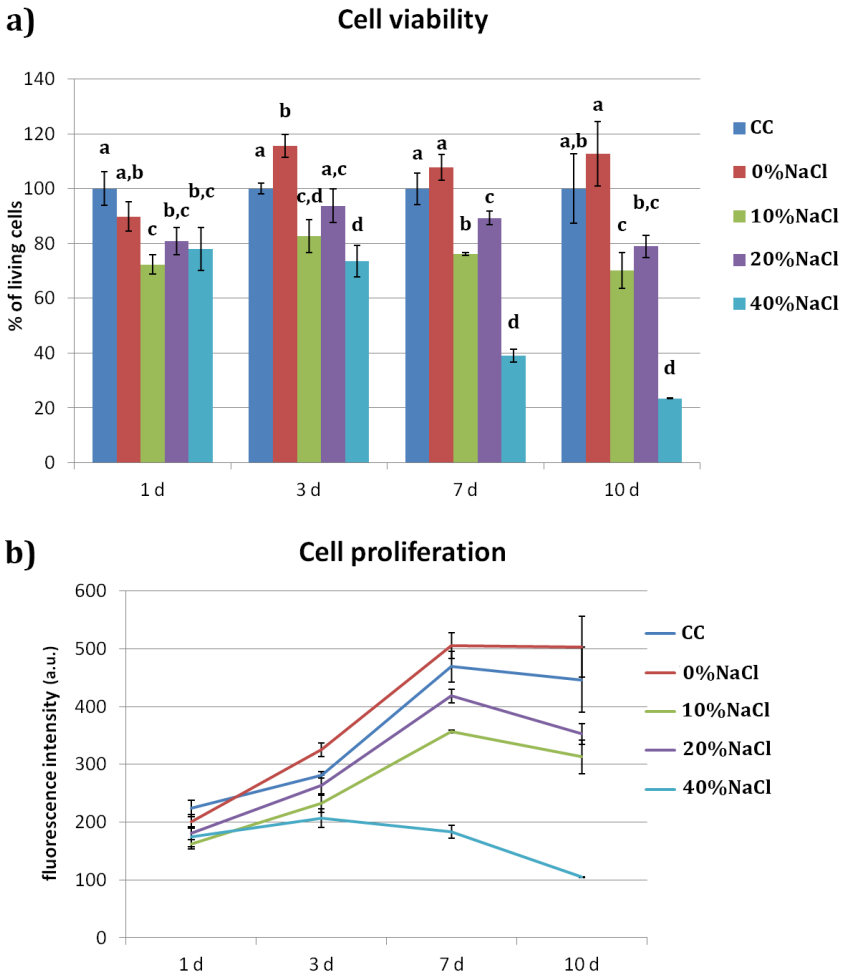

Fig. 14: Cell viability (a) and cell proliferation (b) of Saos-2 cells during 10 days of culture with conditioned media. The percentage of living cells was normalized with control cultures. Arbitrary units (a.u.) were used for cell proliferation. Data are the average of three independent experiments. Significance is represented using an alphabetical superscript system on top of the columns. Letters shared in common among the materials at each time point indicate no significant differences whereas different letters indicate statistically significant differences ($p<0.05$). CC: control cultures.

Table 1: % of porosity and density measured using the Archimedes' principle for the alloys produced with 10, 20 and 40 wt.% of NaCl.

Wt.% NaCl	Porosity (%)	Density (g/cm^3)
10	25.9	5.3
20	41.3	4.2
40	62.3	2.7

Table 2: Young's modulus calculated by nanoindentation at a maximum applied load of 500 mN and Young's modulus calculated using the Gibson-Ashby model for the alloys produced with 10,20 and 40 wt.% of NaCl.

Wt.% NaCl	$E_{nanoindentation}$ (GPa)	$E_{Eq.1}$
10	51.3 ± 2.5	49.3
20	28.5 ± 2.7	32
40	10.2 ± 1	13.2

Table 3: Electrochemical data calculated from the potentiodynamic polarization corrosion tests.

Wt.% NaCl	J_{corr}(A/cm^2)	R_p(Ω•cm^2)	E_{corr} (V vs SCE)
Fe-30Mn6Si1Pd	1.865×10^{-6}	28380	-0.706
Fe-30Mn6Si1Pd-10NaCl	4.466×10^{-6}	21390	-0.737
Fe-30Mn6Si1Pd-20NaCl	2.918×10^{-5}	12570	-0.795
Fe-30Mn6Si1Pd-40NaCl	4.191×10^{-5}	11820	-0.846

Supporting Information

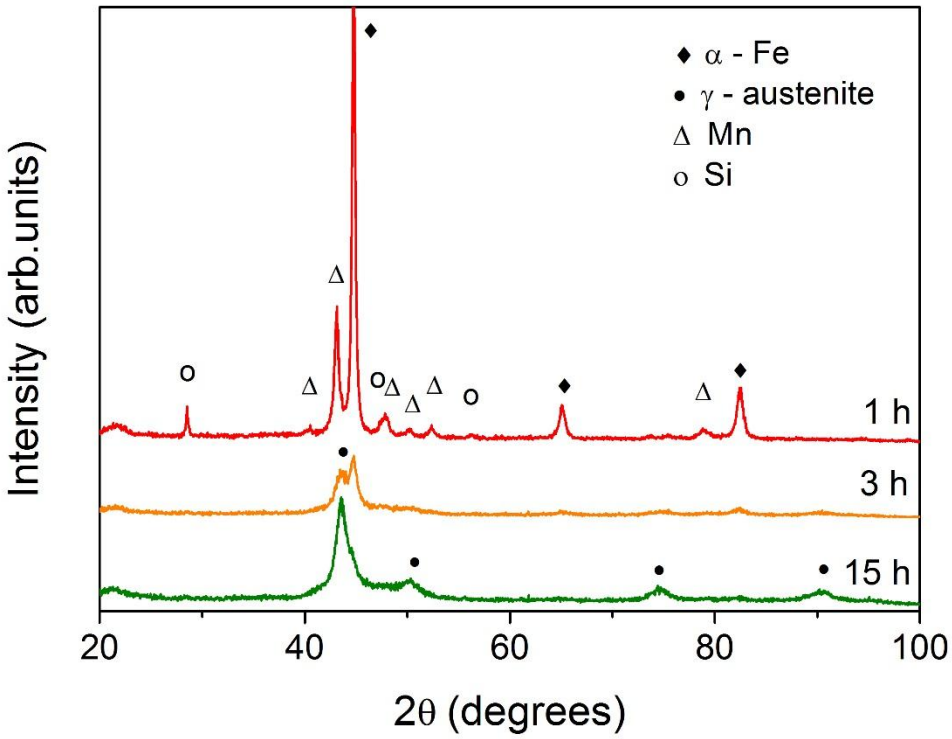

Fig. S1: XRD of the Fe-Mn-Si-Pd powders after 1, 3 and 15 hours of milling.

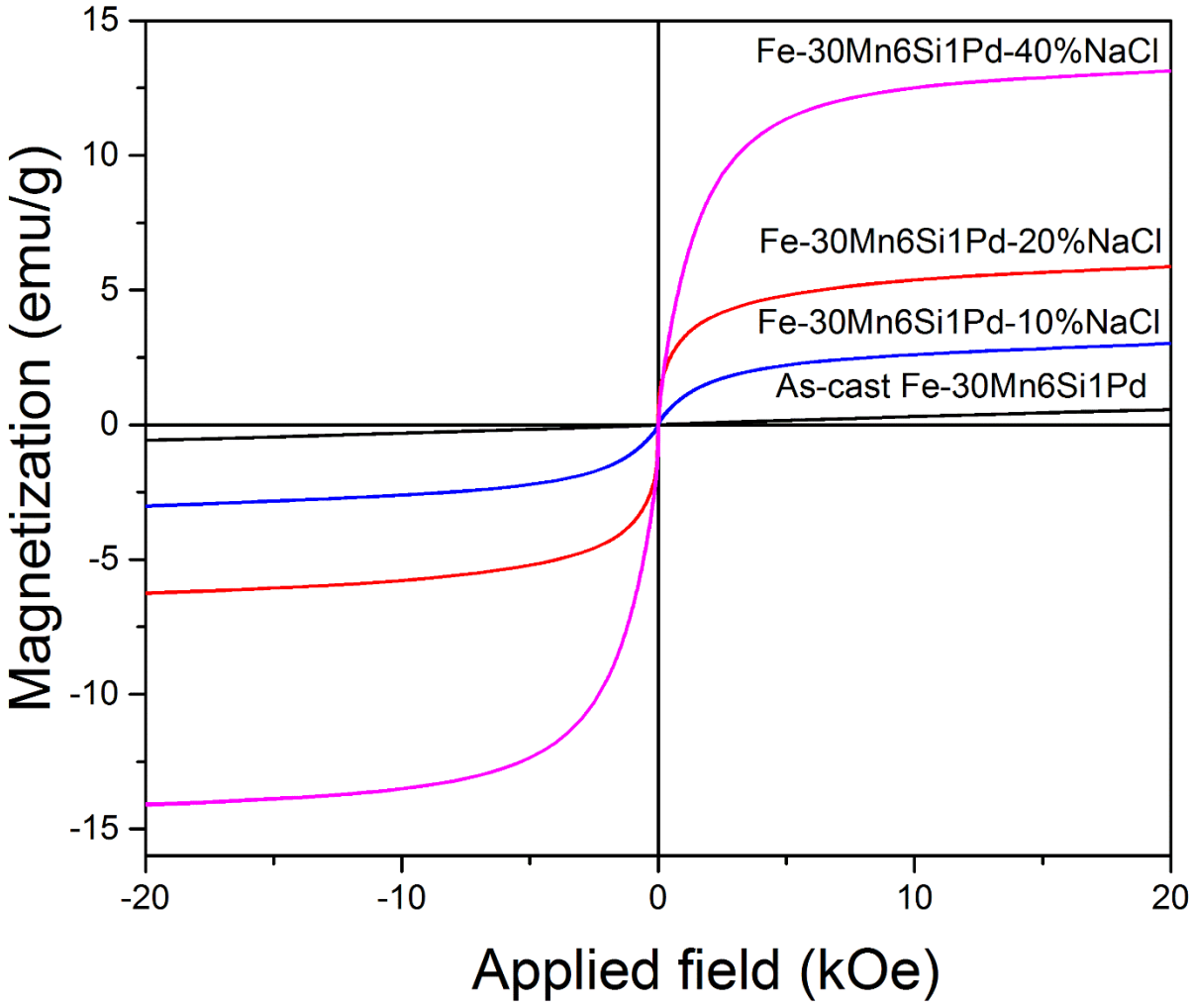

Fig. S2: Dependence of the magnetization as a function of applied magnetic field for fully-compact, as-cast Fe-30Mn6Si1Pd and porous Fe-30Mn6Si1Pd-10%NaCl, Fe-30Mn6Si1Pd-20%NaCl and Fe-30Mn6Si1Pd-40%NaCl alloys after immersion in Hank's solution for 30 days.

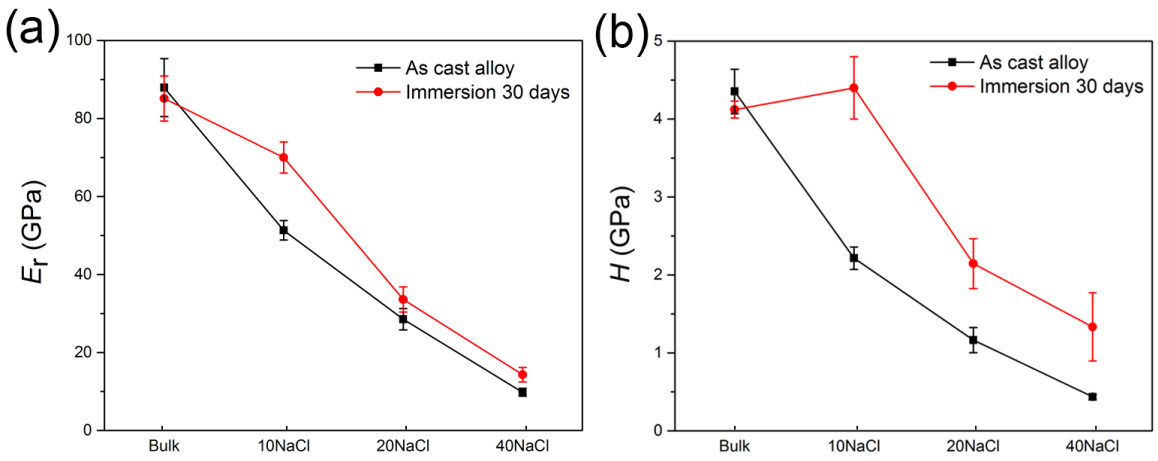

Fig. S3: Reduced Young's modulus (E_r) and hardness (H) for as-prepared Fe-30Mn6Si1Pd, Fe-30Mn6Si1Pd-10%NaCl, Fe-30Mn6Si1Pd-20%NaCl and Fe-30Mn6Si1Pd-40%NaCl before and after immersion in Hank's solution for 30 days.

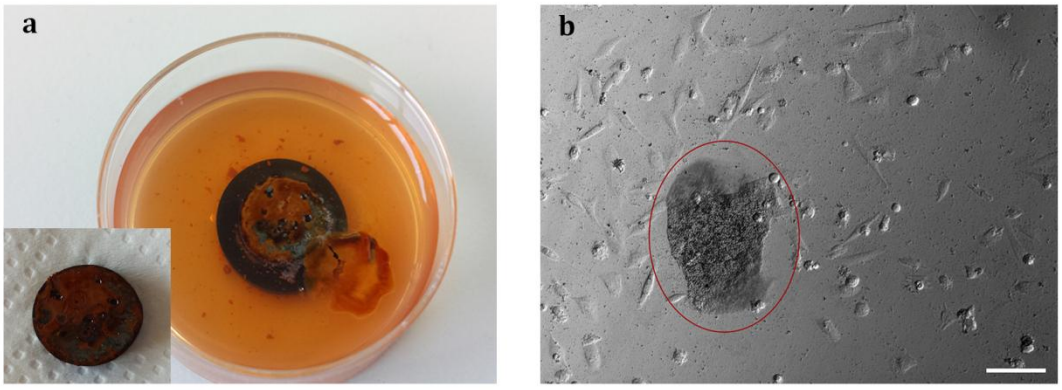

Fig. S4: Alloy surface degradation 24 h after cell seeding: (a) macroscopic view of Fe-30Mn6Si1Pd-40%NaCl alloy degradation (b) debris released from Fe-30Mn6Si1Pd-10%NaCl alloy under an inverted microscope. The inset in (a) shows the formation of an heterogeneous corrosion layer on the alloy surface.

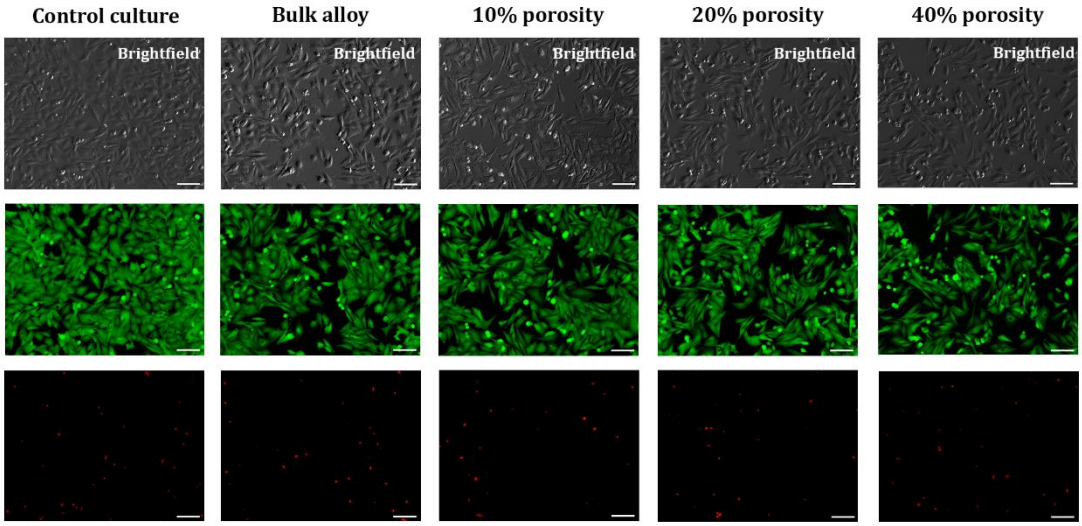

Fig. S5: Living (green) and dead (red) cells after 24 h of cell culture with conditioned medium. A confluent cell monolayer can be seen in control culture whereas cultures incubated with conditioned medium formed subconfluent monolayers. Images were obtained under a flourescence microscope. Scale bar: 100 µm.